DOI: ADD DOINUMBER HERE

Numerical and Experimental Investigation of a Lab-Scale Paraffin Motor with Swirled Injection of Gaseous Oxygen

Mario Tindaro Migliorino[⋆†], *Marco Fabiani*[⋆], *Christian Paravan*[⋆⋆], *Daniele Bianchi*[⋆]
Francesco Nasuti[⋆], *Luciano Galfetti*[⋆⋆], *Rocco Carmine Pellegrini*[⋆⋆⋆], *Enrico Cavallini*[⋆⋆⋆]
[⋆]*Sapienza University of Rome*
00184 Rome, Italy
mariotindaro.migliorino@uniroma1.it · m.fabiani@uniroma1.it
daniele.bianchi@uniroma1.it · francesco.nasuti@uniroma1.it
[⋆⋆]*Politecnico di Milano*
20133 Milan, Italy
christian.paravan@polimi.it · luciano.galfetti@polimi.it
[⋆⋆⋆] *Agenzia Spaziale Italiana*
00133 Rome, Italy
rocco.pellegrini@asi.it · enrico.cavallini@asi.it
[†]Corresponding author

Abstract

In this work the regression rate performance and flow physics of a lab-scale hybrid rocket engine burning gaseous oxygen and paraffin-based fuels are experimentally and numerically investigated. Regression rates are obtained by thickness-over-time averaging procedures and through a non-intrusive optical method enabling fuel grain port diameter tracking. A numerical rebuilding of the experimental data is performed with axisymmetric Reynolds-averaged Navier-Stokes simulations, using sub-models accounting for the effects of turbulence, chemistry, radiation and fluid-surface interaction. A fairly good agreement is obtained between the numerical and experimental data.

1. Introduction

Hybrid rocket engines (HREs) are propulsion devices burning a solid fuel and a liquid or gaseous oxidizer [1]. Despite being known since the 1930s [2], they have found limited applications in the past, mainly due to the low fuel regression rate [3], which limited the maximum thrust obtainable with an engine of given size and to the low combustion efficiency, due to the propellants being stored in separate phases. In the past years, however, significant improvements have been made in the field of hybrid propulsion, leading to a renovated interest of the industry, as testified by the flights of SpaceShipOne and Two [4] and by many European efforts, such as the SL1 launcher by Hympulse [5], the work of T4i [6] and the EU 2020 HYPROGEO [7] and ESA's FLPP programs [8].

Among the recent steps of hybrid propulsion the most important was the introduction of liquefying fuels, namely fuels that form an unstable liquid layer on the burning surface, leading to droplet entrainment and to an increase in regression rate [9, 10]. The most common liquefying fuel is paraffin wax, which allows to increase the regression rate up to 3-4 times with respect to conventional pyrolyzing fuels [11], while being cheap, easily available, safe and environmentally friendly [4].
Paraffin wax has, however, low mechanical properties, requiring to be blended with reinforcing agents, such as thermoplastic and thermosetting polymers [12, 13, 14, 15]. In this work, a thermoplastic polymer whose chain is composed by styrene, ethylene, styrene and butylene grafted with maleic anidride (SEBS-MA) is selected. A thorough rheological and ballistic characterization of the paraffin-SEBS blends has been performed.

To further increase both the regression rate and the combustion efficiency, swirl injection may be used [16], injecting the oxidizer into the combustion chamber with a non-zero tangential component of velocity. It is in fact known that, in inert flows, swirl considerably increases the convective wall heat transfer [17] and it has been also proved to be one of the most effective means to increase flame stability and combustion efficiency in combustors and liquid rocket engines [18, 19]. Each swirling flow is characterized by its rotational intensity, quantified by a dimensionless

parameter, the *swirl number* [18], defined as

$$SN = \frac{\text{angular momentum flux}}{R_{\text{wall}} \times \text{axial momentum flux}} = \frac{\int_S (\rho u w r) dS}{R_{\text{wall}} \int_s (\rho u^2) dS} \tag{1}$$

where S is the cross section, r the distance from the axis, R_{wall} the wall radius, ρ the density, u the axial velocity and w the tangential velocity. This parameter is usually rewritten as a *geometric swirl number*, function of the sole geometry of the injector [20, 21]

$$SN_g = \frac{\pi (R_{\text{wall}} - r_h) R_{\text{wall}}}{A_{\text{inj}}} \tag{2}$$

where r_h is the radius of the injection channels and A_{inj} the injection area. This quantity allows to estimate the rotational intensity of the flow near the injection section, before the effects of friction [22], mass adduction and energy release [23] and flow acceleration [24] lead to its rapid decrease. It is known that SN_g is usually an overestimation of the real value of SN [25] due to the simplifying hypotheses [21] made in its definition.
Several firing tests [26, 27, 28, 29, 30] have shown that the use of swirl injection leads to a considerable increase in regression rate, but there is still a relatively incomplete understanding of the relevant physical phenomena. In particular, CFD simulations can be a useful tool in the analysis and design of swirl-injected HREs, providing insight on the internal flowfield and allowing to investigate different configurations without the need for complex and costly experiments. In this work an axisymmetrical numerical model, including the effects of gas-surface interaction, turbulence, chemistry and radiation, is validated through the rebuilding of experimental data. Such simulations can be used as a quick design tool, while, on the other hand, most of the work present in literature either employs 3D [24, 31] or LES [32] simulations, which have high computational cost, or makes use of simplified injection approaches [33].

In this paper, numerical efforts from Centro Ricerca Aerospaziale Sapienza (CRAS) of Sapienza University of Rome are joined with experimental investigations performed at the Space Propulsion Laboratory (SPLab) of Politecnico di Milano, in the framework of the PHAEDRA (Paraffinic Hybrid Advanced Engine Demonstrator for Rocket Application) project coordinated by the Italian Space Agency [34]. The work focuses on the analysis of the ballistics of paraffin-based fuels in a lab-scale hybrid rocket engine.

2. Experimental Setup and Results

Burning tests are performed with a lab-scale hybrid rocket engine extensively described in Ref. [35]. Cylindrical grains with single central port perforation are tested. The experimental setup design enables sample head-end visualization during the burning. The main observable of interest is the solid fuel regression rate ($\dot{r}$). The latter is determined by thickness over time (TOT) method or by an optical time-resolved technique implemented at SPLab [36].

The oxidizer is injected by eight radial channels. The injector features $SN_g = 3.3$. Tested samples initial port diameter (D_0) is 5 *mm*, while the grain external diameter is 30 *mm*, thus, solid fuel web thickness is 12.5 *mm*. Fuel grain length is 50 *mm*. Combustion tests are performed with gaseous oxygen (GOX). Strand ignition is achieved by a solid propellant primer charge. Combustion chamber pressure is measured by a piezoresistive transducer placed in the engine pre-combustion chamber. The oxidizer mass flow rate $\dot{m}_{ox}$ is measured and controlled by a digital flowmeter. Tests are executed with oxidizer mass flow rate in the range 5 to 7.5 g/s.

2.1 Regression Rate Data Reduction

Regression rate data reduction aims at the identification of a relationship between the regression rate and the oxidizer (or propellant) mass flux (G_{ox}, or G respectively). The $\dot{r}(G_{ox})$ is typically presented as a compact power law:

$$\dot{r}(G_{ox}) = a_r \cdot G_{ox}^{n_r} \tag{3}$$

Under given operating conditions, different data reduction methods may imply differences in the $\dot{r}$ values. In spite of this, the relative ballistic grading of the investigated fuel formulations is typically independent of the used data reduction technique.

Thickness Over Time Method
Thickness over time provides time- and space-averaged regression rates. The method is applied on both diameter and

mass changes in the burning time (Δt_b). The latter is defined based on combustion chamber pressure history [35]. Ignition is conventionally set at the time the combustion chamber pressure (p) increases due to the primer charge ignition. Burning test termination is achieved by a nitrogen purge commanded by electrovalves switching from oxidizer to inert gas flow. After ignition, Δt_b is in the range 3 to 5 s for all the performed tests. Given the different fuel regression rates, burning times are tailored to grant suitable average oxidizer mass fluxes for the relative grading of the formulations.
When based on port size change, the regression rate is expressed as the difference between the sample actual initial and final diameters [$D(t_{in})$ and $D(t_{end})$, respectively],

$$\dot{r}_{DD} = \frac{1}{\Delta t_b} \frac{D(t_{end}) - D(t_{in})}{2} \tag{4}$$

In the case of the mass balance, considering the theoretical maximum density (TMD), and the average fuel grain length (L_{grain}), the regression rate is given by

$$\dot{r}_{MB} = \frac{1}{\Delta t_b} \frac{2 \cdot [m(t_{in}) - m(t_{end})]}{TMD \cdot \pi \cdot [D(t_{in}) + D(t_{end})] \cdot L_{grain}} \tag{5}$$

For both Eq.4 and Eq. 5, the corresponding average oxidizer mass flux is defined as

$$\bar{G}_{ox,ave} = \frac{16 \cdot \dot{m}_{ox}}{\pi \cdot [D(t_{end}) + D(t_{in})]^2} \tag{6}$$

Time-resolved Method
The SPLab time-resolved method for the regression rate (TR) is based on high-speed video recording of the combustion process [36]. The regression rate is determined based on the central port diameter sampling. Regression surface tracking starts from the frame the head-end central port diameter became visible at (after primer charge ignition). Data sampling is extended until the end of the combustion (depending on visualization quality). Diameter sampling is performed with frequency in the range 2 to 10 Hz. Higher frequencies are used in the earlier phases of the burning process (faster regression rates), while slower samplings characterize the last part of the measurement (when surface regression is slowed down). During the combustion, central port diameter is sampled along different radial directions (depending on combustion uniformity). The local diameters were averaged to provide the instantaneous diameter at the given sampling time ($\bar{D}_i$). This diameter is considered uniform for the whole specimen length (given the relatively short grain longitudinal extension). The sequence of the $\bar{D}_i$ is a discrete information in time. This discrete sequence of sampled diameters and sampling times is made a continuous function by a power-law fitting

$$\bar{D}(t) = a_D \cdot (t - t_0)^{n_D} + D_0, t \geq t_{ign} \tag{7}$$

The fitting of the Eq. 7 is maximized by the use of the ad hoc defined ignition time (t_{ign}). The latter well suits to the ignition conditions at small scale for the range of initial G_{ox} of interest[37]. The regression rate and oxidizer mass flux histories in time are evaluated starting from Eq. 7 as

$$\dot{r}(t) = \frac{1}{2} \cdot \frac{dD(t)}{dt} = \frac{1}{2} \cdot a_D \cdot n_D \cdot (t - t_0)^{n_D - 1} \tag{8}$$

$$G_{ox}(t) = \frac{4 \cdot \dot{m}_{ox}}{\pi \cdot [\bar{D}(t)]^2} \tag{9}$$

Consistency checks are applied for the evaluation of the time-resolved values, details are reported in Ref. [36]. The time-resolved method provides a regression rate characterization over a G_{ox} range with a single combustion run. Yet, different tests performed for the same fuel under fixed operating conditions can be collapsed in an ensemble average curve. For the latter, uncertainties are evaluated by considering confidence intervals with 95% accuracy. A minimum of three tests are considered for error bar definition in the ensemble average.

2.2 Tested Fuels and Pre-burning Characterization

Tested fuel formulations are based on a commercial microcrystalline wax (SASOL 0907, TMD = 929 kg/m^3 here labeled as mWA). Paraffin is tested as it is, or blended with SEBS-MA (Sigma-Aldrich, TMD = 910 kg/m^3). Carbon powder (Sigma Aldrich, average particle size < 20 μm) is added to all the tested fuels (1 $wt\%$) to prevent in-depth absorption of radiation heat transfer. The styrene copolymer is added to the compositions with mass fractions of 10 and 20 $wt\%$. Details on the tested fuel formulations are given in Table 1.

Table 1: Tested fuel formulations.

Fuel Id.	**Composition**	**TMD,** kg/m^3
F1	mWA (99 *wt%*) + C (1 *wt%*)	929
F2	mWA (89 *wt%*) + SEBS-MA (10 *wt%*) + C (1 *wt%*)	928
F5	mWA (79 *wt%*) + SEBS-MA (20 *wt%*) + C (1 *wt%*)	926

Preliminary thermal and mechanical characterizations of the tested fuels are reported elsewhere [38]. In this work, focus is on the melt fuel rheology due to its impact on the regression rate. Rheology tests are performed to determine the melt fuel viscosity (η) under reference conditions (strain rate range 1-1000 s^{-1}, temperature 423 K).

Blending of mWA with SEBS-MA produces no significant effects on the TMD of the tested formulations. The same holds for the actual densities of the manufactured fuels, that are all within a ±3% of the theoretical value. On the other hand, the impact of the reinforcing polymer on the melt fuel viscosity is marked, as testified by the data reported in Table 1. Cold flow visualizations at ambient pressure for melt layer temperature of 423 K are shown in [35]: viscosity enhancement from F1 to F5 gradually suppresses the melt layer instability, with SEBS-MA addition at 20 *wt%* suppressing droplet detachment from the surface roll waves.

2.3 Ballistic Characterization

Ballistic characterization is presented considering the TOT methods first, then time-resolved data are discussed.
Mass-based TOT shows faster regression rates than the DD counterpart. This is due to the head-end burning altering the grain length: the mass change accounts for this effect that is not captured by the simple diameter measurement. The increasing viscosity due to the SEBS-MA load implies a regression rate reduction of the blended fuel. Entrainment mass transfer suppression is the main cause for the slower recession of the surface. Focusing on F2, the percent regression rate difference (with respect to F1) is -43% when considering DD, and -47% for MB. For F5, the relative grading yields a -63% with DD, and -65% when using the MB method.
A deeper comparison of the ballistic responses of the fuels is possible by the power law fitting reported in the Table 2. Thickness over time data for F1 feature relatively low data fitting values due to the data scattering induced by the fuel mechanical properties. Independently from the reduction method (MB or DD), the n_r value of the power law fitting is close to the value of 0.6 typically found in the literature for the combustion of paraffin wax fuels [9]. The DD data feature a good agreement with the TR counterpart, as shown in Figure 1. In the high G_{ox} region, Eq. 3 shows a relatively low fitting to the instantaneous data. This is an effect of the small port diameter of the samples inducing a relatively strong sensitivity to oxidizer mass flux in the earlier phases of the combustion process.

Table 2: Power law approximations (Eq. 3) TOT and TR data. Thickness over time extends over the G_{ox} range 19 to 85 $kg/(m^2 s)$, while for TR, the investigated interval extends from 19 to 140 $kg/(m^2 s)$.Data are nondimensionalized with respect to those of pure paraffin obtained with DD reduction method.

Fuel Id.	**Technique**	$a_r/a_{r,ref}$	n_r	**Data Fitting**
F1	MB	1.413 ± 0.270	0.587 ± 0.049	0.941
	DD	1.000 ± 0.286	0.600 ± 0.071	0.921
	TR	1.127 ± 0.00(3)	0.567 ± 0.001	0.999
F2	DD	0.428 ± 0.048	0.648 ± 0.029	0.981
F5	DD	0.214 ± 0.024	0.729 ± 0.033	0.986
	TR	0.262 ± 0.00(1)	0.929 ± 0.001	0.988

3. Computational Model and Setup

The numerical simulations have been performed solving the Reynolds–averaged Navier–Stokes (RANS) equations [39], with submodels accounting for the effects of turbulence, chemistry, gas-surface interaction and thermal radiation. The details of the numerical model are reported in [40]. In all simulations an axisymmetric approach has been used, with a periodic boundary condition ensuring the symmetry of the flow. As described in [40], the fluid-surface

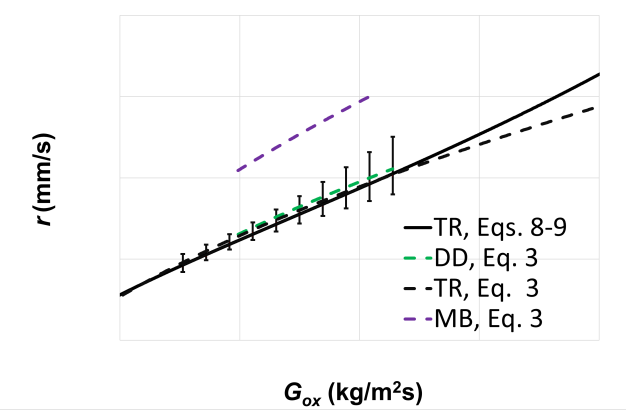

Figure 1: F1 ballistic characterization: time-resolved and TOT data.

interaction sub-model regarding pure paraffin is based on mass and energy balances, which reduce to

$$q_{w,\mathrm{conv}} + q_{w,\mathrm{rad}} = \dot{r}\rho_s \left[\Delta h_{\mathrm{melt}} + c_s(T_{\mathrm{melt}} - T_{s,\mathrm{in}})\right] \tag{10}$$

where $q_{w,\mathrm{conv}}$ and $q_{w,\mathrm{rad}}$ are the convective and radiative wall heat fluxes, $\dot{r}$ the fuel regression rate and the paraffin density, melting enthalpy, specific heat, melting temperature, and initial temperature are, respectively, $\rho_s = 929$ kg/m^3, $\Delta h_{\mathrm{melt}} = 169.83$ kJ/kg, $c_s = 1946.03$ J/(kg·K), $T_{\mathrm{melt}} = 343$ K and $T_{s,\mathrm{in}} = 298.15$ K. The dynamic viscosity of pure paraffin has been experimentally measured.

The computational setup used for the rebuilding of the experimental data is shown in Fig. 2. The combustion chamber is made of a swirl injector ($0 < x < x_0$), a prechamber ($x_0 < x < x_1$), the paraffin grain ($x_1 < x < x_3$), a postchamber ($x_3 < x < x_4$) and a converging/diverging nozzle ($x_4 < x < L$). The latter is composed by conical sections connected by circular arcs with each other and with the cylindrical postchamber. On the left-hand side of the setup an isothermal boundary condition is imposed, with temperature equal to the oxidizer injection temperature. The injector is simulated with a subsonic inflow boundary condition, imposing mass flow rate and static temperature. The discrete tangential injectors of the experimental setup have been substituted with an equivalent annular injector. In an axisymmetric approach it is not possible to inject the flow tangentially, thus either a radial or an axial injector have to be used. Given the geometry of the experimental setup it has been deemed more appropriate to inject the flow radially, but, being the prechamber long, it is expected that the details of the injector have little influence on the fuel regression rate. The width of the injector has been chosen to match the experimental injection area and the flow injection angles are set to obtain a given geometric swirl number. The fuel grain boundary condition is based on the mass and energy balance equations, while the postchamber and nozzle walls are modeled with an adiabatic boundary condition. On the centerline a symmetry boundary condition is imposed and a supersonic outlet is assumed at nozzle exit. On the lateral faces a periodic boundary condition is imposed to model the axisymmetric swirling flow.

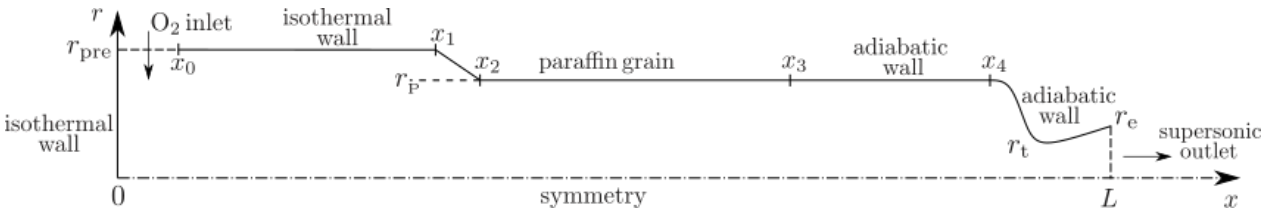

Figure 2: Computational setup.

The prechamber-grain transition has been approximated with a 60° inclined line, since the experimental results show that the inclination of the front-facing end of the grain varies between 90° and 45° during the burn. The postchamber radius has been assumed equal to the port radius, since the postchamber affects mainly pressure and combustion efficiency, which are not the main focus of the present work.

Simulations taking into account the variation of fuel grain shape during the burning time have also been performed. This *shape change* approach simulates the entire firing test of the engine with a series of steady-state simulations in which the shape of the propellant grain is adjourned at each time step, taking into account the regression rate previously computed. This approach is made possible by the characteristic times of grain regression being significantly larger than the ones of the gasdynamic and chemical phenomena inside the engine.

The structured grid employed in the computations is made of 400×120 cells, with clustering near the injector, at the prechamber-grain transition and at the nozzle throat.

4. Numerical Results

The average regression rates computed from the simulations for the F1 formulation are shown in Fig. 3 together with their least square fit. With respect to simulations with axial injection ($SN_g = 0$) the use of swirl injection allows a far better rebuilding of the experimental data. Three simulations have been performed at $r_P = 5$, 6.5 and 7.3 mm respectively. For all simulations the numerical regression rate is in between the DD and the MB measures, but has a slightly larger n_r exponent. Considering also the experimental uncertainties, the numerically obtained regression rates are in fair agreement with the experimental data.

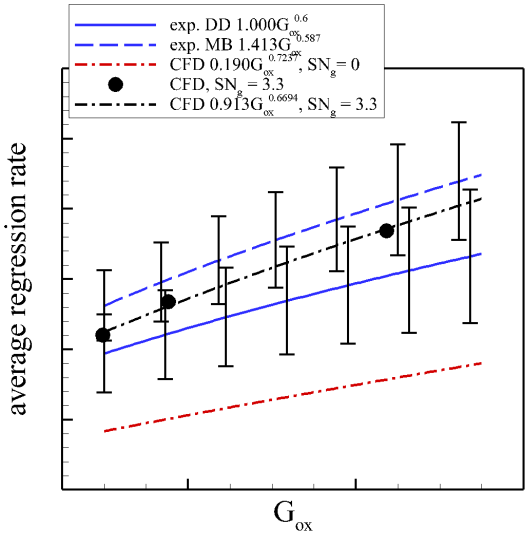

Figure 3: Comparison between experimental and numerical regression rates.

Fig. 4 shows the temperature flowfields of the three simulations. Near the injector two recirculation zones are created, one on the side of the injector and one on the axis, the latter due to the centrifugal forces pushing the flow away from the centerline. A third small vortex is formed just before the prechamber end. The flame is attached at the grain leading edge and quickly grows in thickness. It reaches the engine axis just after the grain end ($x = 0.1273$ m) and a cool layer of gas is formed near the wall up to the nozzle throat.
Fig. 5 shows instead the local regression rate. It can be seen that as the port radius increases the regression rate decreases, since the oxidizer mass flux is lower. The regression rate shows two peaks, one at the grain leading edge, which is the point with minimum boundary layer thickness, and one at $x \approx 0.08$ m, as in a boundary layer reattachment phenomenon. The regression rate increases along x, due the increase in both convective and radiative heat fluxes (Fig. 6(a) and 6(b)). It is also clear that radiation contributes significantly the overall heat flux, especially at higher port radii.

To obtain a more precise rebuilding of the experimental data, one of the firing tests has been rebuilt also with the *shape change* approach. The test has an oxidizer mass flow rate of 6.5 g/s and an initial port diameter of 5 mm.
Looking at the experimental pressure trace it can be seen that the startup transient is quite long, meaning that starting the simulations at the initial grain diameter (5 mm) would probably lead to great errors in the reconstruction. Since the measures taken with the video equipment start at $r_P = 4$ mm, it has been chosen to start the simulations at this port radius, with a reduced burning time of 4.84 s. The time intervals have been chosen according to the computed regression rate: the higher the regression the lower the time interval, for a total of 7 simulations.

The predicted grain profiles are shown in Fig. 7. The experimental axial consuption is 6.8 mm, while the predicted is 5.61 mm (computed at the grain leading edge). A slight underestimation is, however, expected, since the mesh used is composed of a single block, instead of a multiple blocks able to model a vertical wall. In fact, in a single-block simulation the vertical face of the grain is substituted by an inclined one and the resulting boundary layer thickness at the grain leading edge is higher, yielding a reduced heat flux and lower regression rate. Further comparison with the experimental data suggests that the coning of the grain predicted by the simulations may be overestimated, since it is not present in the grain after the burn. This may be due to an overestimation of the radiative heat flux, which is the main cause of the regression rate increase along the grain or to the neglecting of the startup transient and the

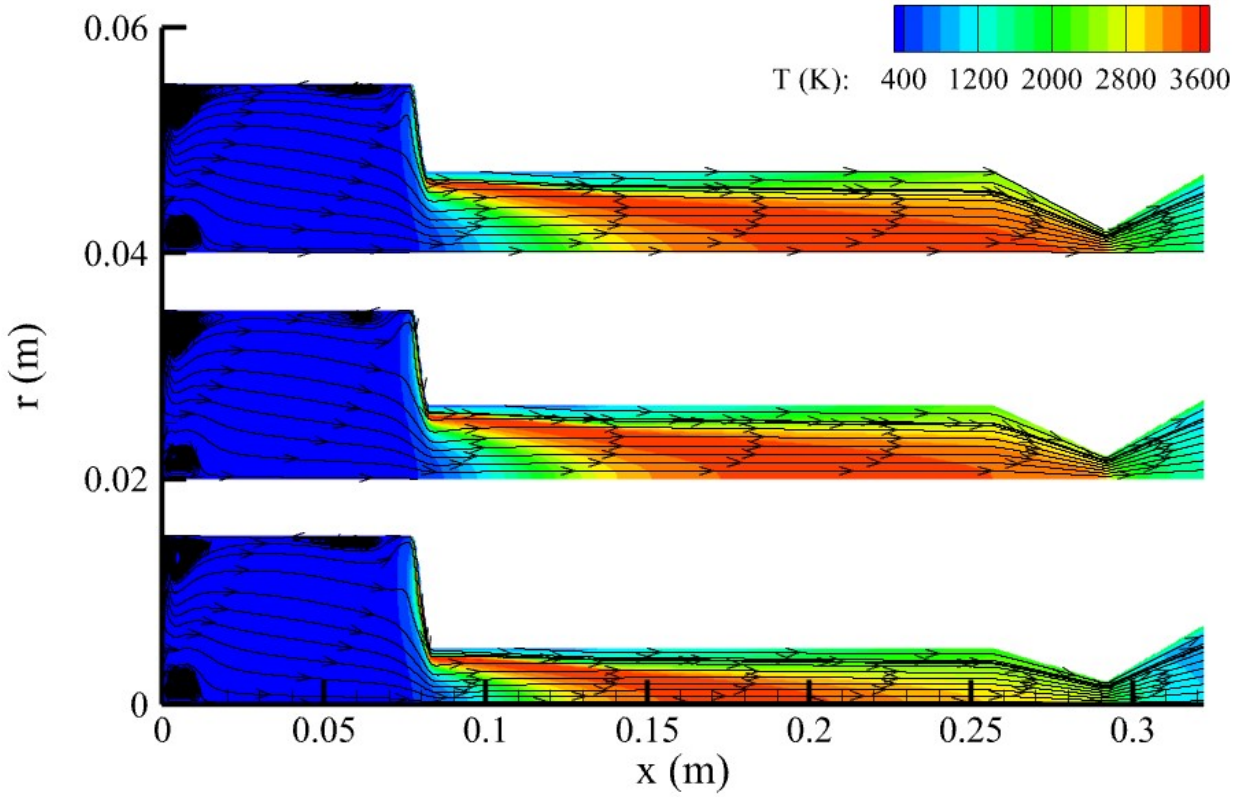

Figure 4: Temperature flowfields for r_p = 5 mm (bottom), 6.5 mm (middle) and 7.3 mm (top).

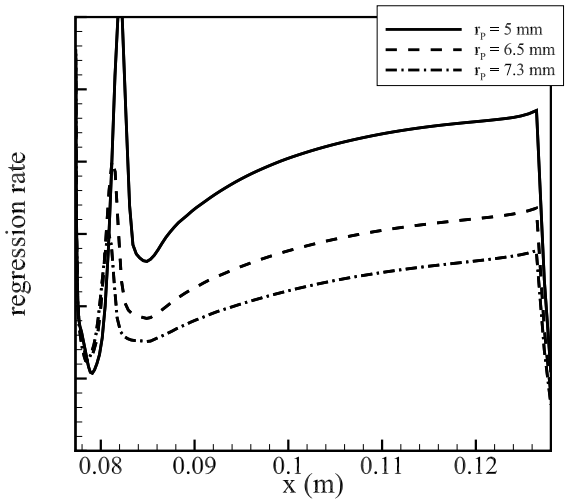

Figure 5: Regression rate profile.

resulting uncertainty on the initial grain shape. From Fig. 7 we can also see that the inclined face becomes steeper during the burn, in contrast with the experimental result of a final face inclination of roughly 45°. The abscissa of the point of minimum diameter, in fact, appears to remain almost constant after t = 0.5 s, explaining why the axial regression leads to an increase of the grain slope. It must be taken into account, however, that the use of a single-block mesh and of smoothing techniques in the grain profile computation do not allow for a precise reconstruction of the grain shape in this region of the grain.

In spite of the geometrical simplifications employed, the average regression rate compares well with the TR

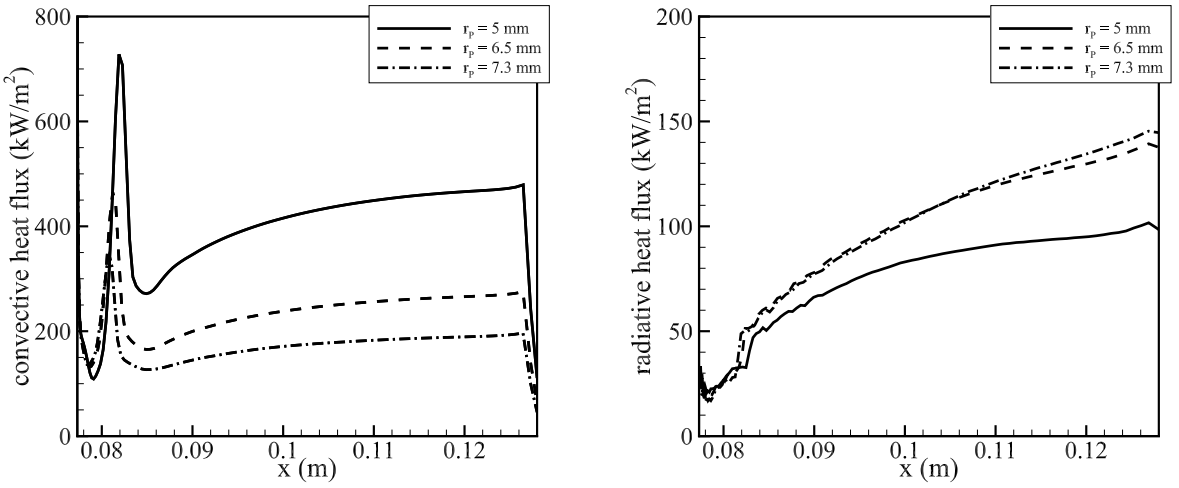

(a) Convective heat flux.

(b) Radiative heat flux.

Figure 6: Wall heat fluxes.

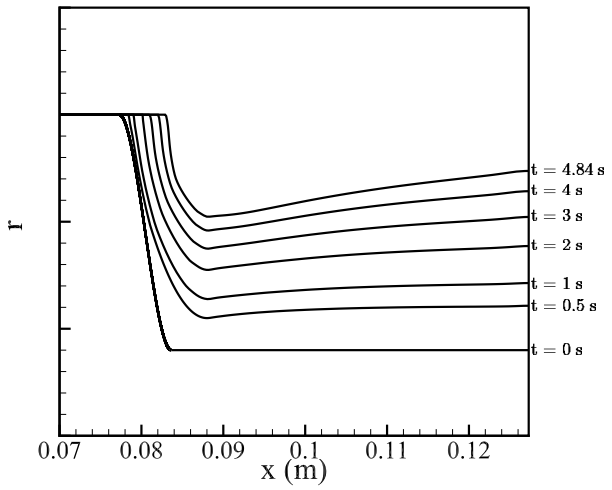

Figure 7: Grain profile evolution over time.

measure (Fig. 8) after t = 1 s, while it is slightly overestimated in the first part of the burn.
A final comparison has been made between the predicted and measured average pressure values. The experimental value (taken on the entire firing test) is 11.38 bar, while the time-average of the CFD simulations is 13.60 bar, with an error of $\approx$ 19.5%. The discrepancy between the two values can be explained by possible occlusions of the pressure sensor and by the inability of the numerical model to take into account the start-up transient of the engine.

4.1 SEBS-MA modeling

The fuel regression rate computed through Eq. (10) depends on (i) the convective heat transfer; (ii) the radiative heat transfer; (iii) the fuel density ρ_s; (iv) the enthalpy of melting Δh_{melt}; (v) the conductive heat transfer $c_s(T_{\text{melt}} - T_{s,\text{in}})$. The convective heat transfer depends on the liquid isobaric specific heat, the dynamic viscosity and the thermal conductivity (c_p, μ, k), while the radiative heat transfer depends on the grain's radiation emissivity.

The effect of the addition of SEBS on the fuel density and the melting temperature has been observed to be negligible from experimental measurements (hence ρ_s, T_{melt}, $T_{s,\text{in}}$ are kept as the ones of F1 paraffin). Moreover, the

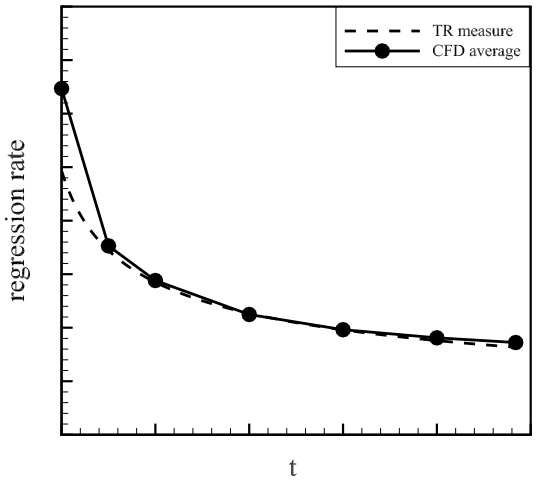

Figure 8: Comparison between numerical and time-resolved regression rate.

radiation emissivity is not expected to influence significantly the regression rate [41].

The dynamic viscosities of the liquefied paraffin of the three formulations (F1, F2, F5) have been measured for different temperature ranges and are reported in Fig. 9. The asymptotic behavior correlation (ABC) values of [42] are multiplied by appropriate factors (2.8 for F1, 23 for F2, and 80 for F5) in order to reproduce the measured viscosities. Liquid specific heat and thermal conductivity were however not measured and are here assumed to be equal to the ones of the ABC model for all fuel formulations. The sensitivity of the regression rate to these two fuel properties has been assessed as negligible if they vary of 5-10%, which is expected given the dominance of paraffin in the fuel.

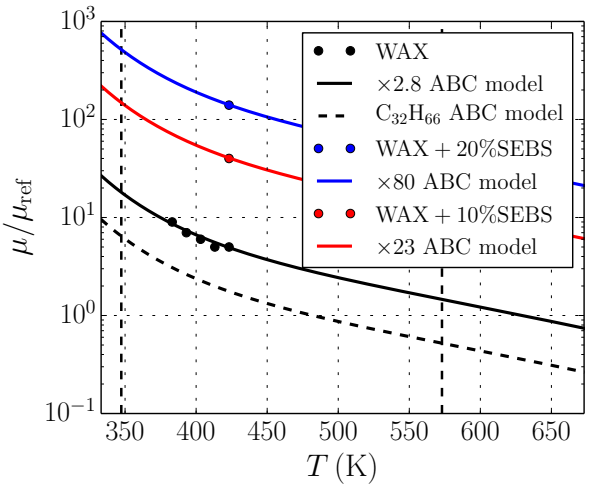

Figure 9: Dynamic viscosity of F1, F2, and F5 fuel formulations from measurements (symbols) and model of [42] (dashed and solid lines).

Properties of the solid fuel that strongly affect the regression rate in Eq. (10) are c_s and Δh_{melt}, which are however not known due to lack of experimental and literature data. The first one can be computed with a weighted average of wax and SEBS properties,

$$c_s = y_{\text{SEBS}}\, c_{s,\text{SEBS}} + (1 - y_{\text{SEBS}}) c_{s,\text{wax}} \tag{11}$$

where $y_{\text{SEBS}} = 0$, 0.1, and 0.2 for F1, F2, and F5 formulations, respectively, and $c_{s,\text{SEBS}}$ is unknown.

Modeling of wax-SEBS blends should theoretically take into account the different nature of the two fuels (liquefying and pyrolyzing), which is outside the scope of this work. On the other hand, in order to compute Δh_{melt}, it is here assumed that the pyrolysis of SEBS takes place simultaneously to the melting of the paraffin grain. In this way, Δh_{melt}

is obtained as a weighted average of the heat of melting of paraffin and the heat of pyrolysis of SEBS,

$$\Delta h_{\text{melt}} = y_{\text{SEBS}} \Delta h_{\text{p}} + (1 - y_{\text{SEBS}}) \Delta h_{\text{melt,wax}} \tag{12}$$

where Δh_{p} is unknown.

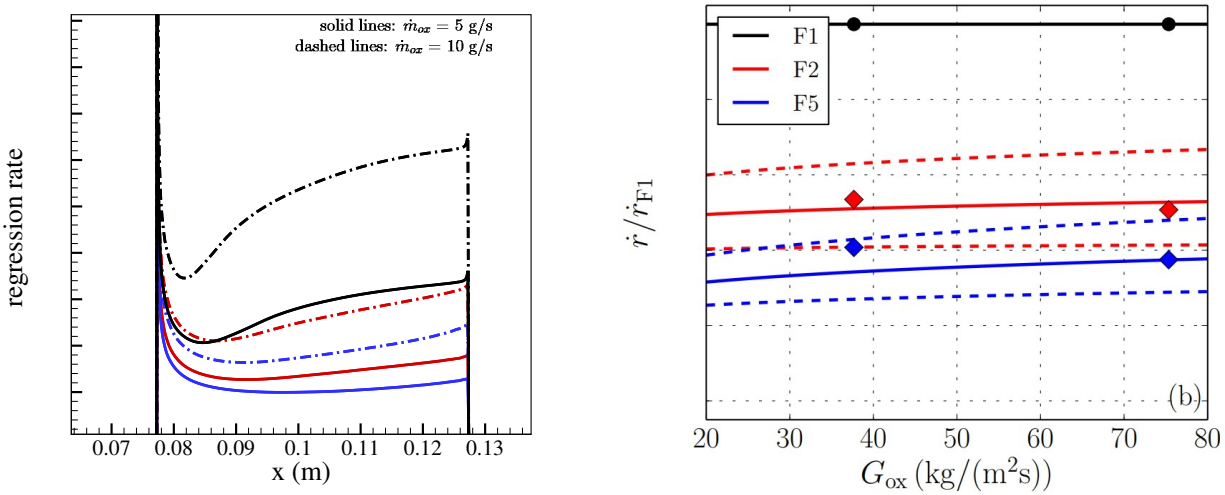

(a) Regression rate profiles over the fuel grain.

(b) Regression rates normalized with the values obtained for the F1 formulation. Symbols indicate numerical results, while lines indicate experimental nominal data (solid lines) with related uncertainty (dashed lines).

Figure 10: Regression rates from simulations at r_p = 6.5 mm and SN_g = 3.3 for F1, F2, and F5 fuel formulations.

Due to lack of experimental and literature data, SEBS values of c_s and Δh_{p} are inferred from comparison between CFD results and experimental data. The main tuning parameter is the term on the right hand side of Eq. (10), which reads

$$\Delta H = \Delta h_{\text{melt}} + c_s (T_{\text{melt}} - T_{s,\text{in}}) \tag{13}$$

Four different simulations at port radius 6.5 mm and SN_g = 3.3 were performed, resulting in the regression rates shown in Fig. 10a. By normalizing the regression rates with the ones obtained with the F1 formulation, it was possible, by adopting $\Delta H_{\text{SEBS}} = 1.7 \Delta H_{\text{HDPE}}$, to fit the data through the experimental trends with good accuracy (Fig. 10b). It is remarkable that, despite of the modeling assumptions, a single tuning of ΔH yields an acceptable representation of the regression rate for two different fuel formulations and oxidizer mass flow rates. The individual values of Δh_{p} and c_s are such that $\Delta H_{\text{SEBS}} = 1.7 \Delta H_{\text{HDPE}}$ and are reported in Table 3, where they can be compared with properties of HTPB and HDPE.

Table 3: Values of heat of pyrolysis Δh_{p} and specific heat c_s for different materials.

Material	Δh_{p} **(MJ/kg)**	c_s **(J/(kg· K))**	**Reference**
HTPB	1.1	1632.0	[43, 44]
HDPE	2.72	1255.2	[45]
SEBS	4.624	2133.84	-

A final consideration is to be given to chemical composition of liquefied fuel. To model exactly the behavior of wax-SEBS fuels one should consider not only paraffin, but also styrene (C_8H_8), ethylene (C_2H_4), and butylene (C_4H_8). However, considering the relatively low mass fraction of styrene present in SEBS-MA [46], the overall ratio between carbon and hydrogen atoms is not significantly modified with respect to pure paraffin. Therefore, from the fuel it is assumed that the only species released to the flowfield is $C_{32}H_{66}$. A simulation considering the injection of 10% ethylene with 90% $C_{32}H_{66}$ provided no appreciable change in regression rate with respect to a simulation considering 100% $C_{32}H_{66}$ injection.

5. Conclusions

An experimental and numerical analysis of hybrid rocket engines burning paraffin-wax and gaseous oxygen has been performed, in order to assess the effect of swirl injection on the regression rate.

Tested specimens featured grain lengths of 50 mm, with external diameter of 30 mm and initial port diameter in the range 5 to 20 mm. Firing tests were conducted varying oxygen mass flow rate from 5 to 10 g/s, obtaining average oxidizer mass fluxes in the range 20-60 kg/(m^2·s) and regression rates in the range 0.5 to 2.5 mm/s. Regression rates obtained by classical thickness-over-time (TOT) averaging procedure were compared to fuel time-resolved ballistics. Time-resolved data were obtained by an optical method enabling port diameter tracking.

The numerical approach has been validated through the rebuilding of experimental data at different oxidizer mass fluxes and mass flow rates, yielding satisfactory results. The predictive capabilities of the model have been improved through simulations taking into account the variation of the fuel grain shape during the burn. The inclusion of SEBS into paraffin fuels has been successfully modeled with a simplified approach.

6. Acknowledgments

This work is part of a wider research framework on hybrid rocket propulsion funded by the Italian Space Agency under contract ASI N. 2019-5-I.0, CUP F84E16002240003.

References

[1] G. P. Sutton and O. Biblarz. *Rocket propulsion elements*. John Wiley and Sons, Inc., 2017.

[2] M. J. Chiaverini and K. K. Kuo, editors. *Fundamentals of Hybrid Rocket Combustion and Propulsion*. AIAA, 2007.

[3] D. Pastrone. Approaches to low fuel regression rate in hybrid rocket engines. *International Journal of Aerospace Engineering*, 2012, 2012.

[4] B. Cantwell, A. Karabeyoglu, and D. Altman. Recent advances in hybrid propulsion. *International Journal of Energetic Materials and Chemical Propulsion*, 9:305–326, 2010.

[5] C. Schmierer, M. Kobald, U. Fischer, K. Tomilin, A. Petrarolo, and F. Hertel. Advancing europe's hybrid rocket engine technology with paraffin and LOX. *8th European Conference for Aeronautics and Aerospace Sciences (EUCASS)*, 2019.

[6] T4i technology for propulsion and innovation, https://www.t4innovation.com.

[7] Project: HYPROGEO, EC H2020 Project Number 634534, Hybrid Propulsion Module for Transfer to GEO Orbit,2015 – 2018.

[8] M.G. Faenza, A.J. Boiron, B. Haemmerli, S. Lennart, T. Vesteras, and O. Verberne. Getting ready for space: Nammo's development of a30 kN hybrid rocket based technology demonstrator. *7th European Conference for Aeronautics and Space Sciences (EUCASS)*, 2017.

[9] M. A. Karabeyoglu, D. Altman, and B. J. Cantwell. Combustion of liquefying hybrid propellants: Part 1, general theory. *Journal of Propulsion and Power*, 18(3):610–620, 2002.

[10] M. A. Karabeyoglu and B. J. Cantwell. Combustion of liquefying hybrid propellants: Part 2, stability of liquid films. *Journal of Propulsion and Power*, 18(3):621–630, 2002.

[11] M. A. Karabeyoglu, B. Cantwell, and D. Altman. *Development and testing of paraffin-based hybrid rocket fuels*. 2001.

[12] M. Kobald, C. Schmierer, H. K. Ciezki, S. Schlechtriem, E. Toson, and L. T. De Luca. Viscosity and regression rate of liquefying hybrid rocket fuels. *Journal of Propulsion and Power*, 33(5):1245–1251, 2017.

[13] C. Paravan, L. Galfetti, and F. Maggi. A critical analysis of paraffin-based fuel formulations for hybrid rocket propulsion. *53rd AIAA/SAE/ASEE Joint Propulsion Conference*, AIAA Paper 2017-4830, 2017.

[14] Y. Tang, S. Cheng, W. Zhang, R. Shen, L.T. DeLuca, and Y. Ye. Mechanical modifications of paraffin-based fuels and the effects on combustion performance. *Propellants, Explosives, Pyrotechnics*, 42(11):1268–1277, 2017.

[15] J.C. Thomas, C. Paravan, J.M. Stahl, A.J. Tykol, F.A. Rodriguez, L. Galfetti, and Eric L. Petersen. Experimental evaluation of htpb/paraffin fuel blends for hybrid rocket applications. *Combustion and Flame*, 229:111386, 2021.

[16] S. Yuasa, O. Shimada, T. Imamura, T. Tamura, and K. Yamoto. A technique for improving the performance of hybrid rocket engines. In *35th Joint Propulsion Conference and Exhibit*, 1999.

[17] F. Chang and V.K. Dhir. Mechanisms of heat transfer enhancement and slow decay of swirl in tubes using tangential injection. *International Journal of Heat and Fluid Flow*, 16(2), 1995.

[18] A. K. Gupta, D. G. Lilley, and N. Syred. *Swirl flows*. Abacus Press, 1984.

[19] G. P. Sutton. *History of Liquid Propellant Rocket Engines*. AIAA, 2006.

[20] N. Syred and J.M. Beér. Combustion in swirling flows: A review. *Combustion and Flame*, 23(2), 1974.

[21] T.C. Claypole and N. Syred. The effect of swirl burner aerodynamics on NOx formation. *Symposium (International) on Combustion*, 18(1), 1981. Eighteenth Symposium (International) on Combustion.

[22] F. Chang and V.K. Dhir. Turbulent flow field in tangentially injected swirl flows in tubes. *International Journal of Heat and Fluid Flow*, 15(5), 1994.

[23] K. Ozawa and T. Shimada. Linear combustion stability analysis of uni-directional vortex injection hybrid rocket engines. *50th AIAA/ASME/SAE/ASEE Joint Propulsion Conference*, 2014.

[24] E. Paccagnella, F. Barato, D. Pavarin, and A. Karabeyoğlu. Scaling parameters of swirling oxidizer injection in hybrid rocket motors. *Journal of Propulsion and Power*, 33(6):1378–1394, 2017.

[25] D. R. Greatrix. Geometric swirl number and hybrid rocket engine performance. *2018 Joint Propulsion Conference*, 2018.

[26] S. Yuasa, N. Shiraishi, and K. Hirata. Controlling parameters for fuel regression rate of swirling-oxidizer-flow-type hybrid rocket engine. *48th AIAA/ASME/SAE/ASEE Joint Propulsion Conference*, 2012.

[27] T. Sakurai, S. Yuasa, H. Ando, K. Kitagawa, and T. Shimada. Performance and regression rate characteristics of 5-kN swirling-oxidizer-flow-type hybrid rocket engine. *Journal of Propulsion and Power*, 33(4):891–901, 2017.

[28] F. D. A. Quadros and P. T. Lacava. Swirl injection of gaseous oxygen in a lab-scale paraffin hybrid rocket motor. *Journal of Propulsion and Power*, 35(5):896–905, 2019.

[29] L.-L. Liu, X. He, Y. Wang, Z.-B. Chen, and Q. Guo. Regression rate of paraffin-based fuels in hybrid rocket motor. *Aerospace Science and Technology*, 107:106269, 2020.

[30] M. Franco, F. Barato, E. Paccagnella, M. Santi, A. Battiston, A. Comazzetto, and D. Pavarin. Regression rate design tailoring through vortex injection in hybrid rocket motors. *Journal of Spacecraft and Rockets*, 57(2):278–290, 2020.

[31] N. Bellomo, F. Barato, M. Faenza, M. Lazzarin, A. Bettella, and D. Pavarin. Numerical and experimental investigation of unidirectional vortex injection in hybrid rocket engines. *Journal of Propulsion and Power*, 29(5):1097–1113, 2013.

[32] M. Motoe and T. Shimada. Numerical simulations of combustive flows in a swirling-oxidizer-flow-type hybrid rocket. *52nd Aerospace Sciences Meeting*, 2014.

[33] C. Palani Kumar and A. Kumar. Effect of swirl on the regression rate in hybrid rocket motors. *Aerospace Science and Technology*, 29, 2013.

[34] A. Reina, M.L. Frezzotti, G. Mangioni, A. Cretella, F Battista, L. Galfetti, F. Nasuti, D. Pavarin, R.C. Pellegrini, and E. Cavallini. Hybrid propulsion system for future rocket applications. *Space Propulsion Conference*, 2022.

[35] C. Paravan, L. Galfetti, R. Bisin, and F. Piscaglia. Combustion processes in hybrid rockets. *International Journal of Energetric Materials and Chemical Propulsion*, 18(3):255–286, 2019.

[36] C. Paravan. Nano-sized and mechanically activated composites: Perspectives for enhanced mass burning rate in aluminized solid fuels for hybrid rocket propulsion. *Aerospace*, 12(6):1–31, 2019.

[37] C. Paravan, M. Manzoni, G. Rambaldi, and L. T. DeLuca. Analysis of quasi-steady and transient burning of hybrid fuels in a lab-scale burner by an optical technique. *International Journal of Energetric Materials and Chemical Propulsion*, 13(5):385–410, 2013.

[38] R. Bisin, C. Paravan, S. Alberti, and L. Galfetti. A new strategy for the reinforcement of paraffin-based fuels based on cellular structures: The armored grain — mechanical characterization. *Acta Astronautica*, 176:494–509, 2020.

[39] J. D. Anderson. *Hypersonic and High-Temperature Gas Dynamics*. AIAA Education Series, 2006.

[40] M. T. Migliorino, D. Bianchi, and F. Nasuti. Numerical analysis of paraffin-wax/oxygen hybrid rocket engines. *Journal of Propulsion and Power*, 36(6):806–819, 2020.

[41] M. T. Migliorino, D. Bianchi, and F. Nasuti. Numerical simulations of the internal ballistics of paraffin–oxygen hybrid rockets at different scales. *Aerospace*, 8(8), 2021.

[42] J. J. Marano and G. D. Holder. A general equation for correlating the thermophysical properties of n-paraffins, n-olefins, and other homologous series. 3. Asymptotic behavior correlations for thermal and transport properties. *Ind. Eng. Chem. Res.*, 36(6):2399–2408, 1997.

[43] K. Ramohalli and J. Yi. Hybrids Revisited. AIAA Paper 1990-1962, July 1990.

[44] E. Farbar, J. Louwers, and T. Kaya. Investigation of Metallized and Nonmetallized Hydroxyl Terminated Polybutadiene/Hydrogen Peroxide Hybrid Rockets. *Journal of Propulsion and Power*, 23(2):476–486, 2007.

[45] G. Lengelle, B. Fourest, J. Godon, and C. Guin. Condensed-phase behavior and ablation rate of fuels for hybrid propulsion. AIAA Paper 1993-2413, 1993.

[46] Z.A. Mohd Ishak Kusmono, W.S. Chow, T. Takeichi, and Rochmadi. Compatibilizing effect of sebs-g-ma on the mechanical properties of different types of ommt filled polyamide 6/polypropylene nanocomposites. *Composites Part A: Applied Science and Manufacturing*, 39(12):1802–1814, 2008.